# Breakdown and rearrangement of a vortex street in the far wake of a cylinde

Karasudani, Takashi
Research Institute for Applied Mechanices, Kyushu University : Research Associate

Funakoshi, Mitsuaki
Research Institute for Applied Mechanice, Kyushu University : Associate Professor

https://doi.org/10.5109/6786326

出版情報：Reports of Research Institute for Applied Mechanics. 39 (110), pp.1-27, 1994-02. 九州大学応用力学研究所
バージョン：
権利関係：

Reports of Research Institute for Applied Mechanics
Vol. XXXIX, No. 110,1994

# Breakdown and rearrangement of a vortex street in the far wake of a cylinder

By Takashi KARASUDANI* Mitsuaki FUNAKOSHI†

Breakdown and rearrangement of a primary vortex street shed from a circular cylinder in the far wake are experimentally examined for $70<R<154$ ($R$ is the Reynolds number based on the diameter of the cylinder). According to the vorticity fields obtained using digital image processing for visualized flow fields, the primary vortex street breaks down into a nearly parallel shear flow of Gaussian profile at a certain downstream distance, before a secondary vortex street of larger scale appears further downstream. The process leading to the nearly parallel flow can be explanined as the evolution of the vortex regions of an inviscid fluid if we invoke the observation that the distance between the two rows in the primary vortex street increases with the downstream distance. Numerical computations with the discrete vortex method also support this explanation. Next, the wavelengths, $a_1$ and $a_2$, of the primary and secondary vortex streets are calculated from the above vorticity fields, and are also measured from the flow patterns obtained using the aluminium dust method. The ratio $a_2/a_1$ decreases with increasing $R$, and ranges from 1.7 to 2.6. Moreover, the wavelength $a_2$ is a little smaller than that of the most unstable mode in the linear stability theory applied to the above nearly parallel flow. The speeds of the vortex streets relative to the fluid at infinity are also measured, and are $0.12U-0.19U$ and $0.03U-0.10U$ for the primary and secondary ones, respectively. Here $U$ is the speed of the cylinder.

***Key words*** : Kármán vortex street, far wake, breakdown, vortex dynamics, image processing

## 1. Introduction

The behaviour of the wake of bluff body is one of the most fundamental problems in hydrodynamics, and there are many experimental and theoretical works on this subject. Regarding the wake of a circular cylinder, it is widely known that a regular two-dimensional vortex street (the Kármán vortex street) is generated for about $50<R<180$ if end conditions are appropriately controlled. Here $R$ is the Reynolds number based on the diameter of the

*Research Associate, Research Institute for Applied Mechanices,Kyushu University.
† Associate Professor, Research Institute for Applied Mechanice, Kyushu University.

cylinder. The evolution of this vortex street (called a primary vortex street from now on) in the far wake is interesting because of its close relation to the subject of the interactions among vorticity-concentrating regions, and was experimentally or theoretically investigated by many researchers.

Using the aluminium dust method, Tanada[1] observed that for $60<R<150$ the primary vortex street breaks down at about 50 diameters downstream and that a new vortex street of larger scale (called a secondary vortex street from now on) is subsequently rearranged. He also suggested that this process may be explained by the linear stability theory for the local mean wake profile which changes slowly in the streamwise direction. The downstream distance of the position at which the primary vortex street ceases to persist was measured by Honji[2] from streak patterns visualized by the electrolytic precipitation method.

Moreover, in the experiments with smoke-wire flow visualization and hot-wire anemometry, Cimbala et al.[3, 4] found that the primary vortex street decays rapidly to a parallel shear flow and that for $100<R<160$ a larger-scale structure (the secondary vortex street) can be seen beyond this region of decay. They also claimed that the growth of this structure is due to the hydrodynamic instability of a developing mean wake profile.

On the other hand, from the experiments for $R\lesssim160$ with smoke-wire flow visualization and hot-wire anemometry, Matsui & Okude[5] and Okude & Matsui[6] proposed that the secondary vortex street is formed owing to a pairing (or merging) of the vortices in the primary vortex street. That is, they claimed that the wavelength of the vortex street becomes larger by the pairing of vortex regions without going through a parallel shear flow state.

The breakdown of the primary vortex was examined also by Durgiin & Karlsson[7] when the vortex street was subjected to a deceleration as it approached a large circular cylinder. Using hot-wire anemometry, they found that a stationary wake flow (calm region) is created after the breakdown and develops into a secondary vortex street. This behaviour is similar to the observation by Cimbala et al.[3, 4], although the geometrical arrangements in these two investigations are different. Durgin & Karlsson suggested that the breakdown is qualitatively explained by considering the convection of a concentrated vortex region due to the motion imposed by all the other vortices. They also attributed the creation of the secondary vortex street to changing hydrodynamic stability.

Moreover, it is widely known that we must be careful in predicting unsteady velocity or vorticity fields from visualized flow patterns. For example, in their experiments with the smoke-wire method, Cimbala et al.[4] suggested that in order to accurately discern the flow at some location, the smoke-wire must be placed at a proper distance upstream of that location. Furthermore, Gursul et al.[8] simulated flow visualization of an unsteady wake by computing the streaklines or timelines associated with a few specified vorticity fields. They found that the visualized patterns for the vorticity fields with and without attenuation in the downstream direction are barely distinguishable from one another.

The main purpose of the present paper is to experimentally examine in detail what occurs in the breakdown and the rearrangement of the primary vortex street, with flowvisualization methods of relatively small ambiguity. We carried out two series of experiments described in §2 : in series I, the aluminium dust method was used in order to measure the geometrical configuration of the primary and secondary vortex streets, whereas, in series II, the flow field was visualized by mixing polyethylene particles with water. Then we obtained the development of velocity and vorticity fields using a digital image processing method introduced in §3.

The results are shown in §4 and are summarized as follows : for $70<R<154$, by appropriately controlling end conditions, two-dimensional vortex streets are observed both in the near and far wakes. Furthermore, the primary vortex street breaks down into a nearly parallel shear flow of Gaussian profile at a certain downstream distance, before a secondary vortex street of larger scale appears further downstream. The ratio of the wavelength of the secondary vortex street to that of the primary vortex street decreases with increasing $R$, and ranges from 1.7 to 2.6. Moreover, the speeds of the vortex streets relative to the fluid at infinity are about $0.12U-0.19U$ and $0.03U-0.10U$ for the primary and secondary vortex streets, respectively. Here $U$ is the speed of the cylinder.

In §5, the essential mechanism in the process from the primary vortex street to the nearly parallel flow is discussed. As first suggested by Durgin & Karlsson[7], this process can be explained as the evolution of vortex regions of an inviscid fluid if we invoke the observation that the distance between the two rows in the primary vortex street increases with the downstream distance. That is, the viscous effect is not dominant in this process. Numerical computations with the discrete vortex method also support this explanation. In §6, the formation of the secondary vortex street is discussed. The wavelength of the secondary vortex street measured in the experiments is compared with the result of the linear stability theory applied to the above nearly parallel flow. Consequently, the measured wavelength is a little smaller than that of the most unstable mode.

There are a few more investigations related to the present work. For example, Matsui & Okude[9] and Okude & Matsui[6] experimentally examined the development of the far-wake flow pattern when a disturbance is introduced into the wake by a loudspeaker. Another experiment involving forcing was carried out by Nakano & Rockwell[10] by oscillating a cylinder transversally. Theoretical investigations of the long-time evolution of a parallel wake flow were performed for an inviscid fluid by Aref & Siggia[11] and by Meiburg[1], whereas the evolution from a regular vortex street of finite area was examined by Tsuboi & Oshima[13]. Maekawa et al.[14] numerically studied the transition mechanism in a spatially developing wake of a viscous fluid. The relation of the results of these experimental and theoretical investigations with the present results is discussed in §§5 and 7.

A preliminary report on a part of the present work was also writted by Karasudani et al.[15]

## 2. Experimental setup

Two water tanks with glass sides were used in the present experiments. The first tank (long tank) is 10m long, 60cm deep, and 60cm wide, whereas the other tank (short tank) is 4m long, 40cm deep and 40cm wide. Over these tanks, rails are mounted horizontally. The long tank has two carriages which are driven by servomotors and move uniformly along the rails. The short tank has a carriage driven by an induction motor. Each tank has a heating device to make the water near the surface thermally stratified and to prevent thermal convection due to evaporation at the surface. This device is an electrical heating wire covered with a polytetrafluoroethylene tube and stretched around near the wall of the tank at about 2cm below the surface.

Each of four stainless steel circular cylinders, one 0.599cm in diameter and 48cm long, another 0.799cm and 56cm, another 0.998cm and 56cm, and the other 1.001cm and 40cm was used as a model. These cylinders were held vertical and towed at speed $U$. The range of the Reynolds number $R$ in the experiments is $70<R<154$. Here $R=Ud/\nu$, $d$ is the diameter of the cylinder, and $\nu$ is the kinematic viscosity of water. It is widely known that end conditions must be appropriately controlled so that two-dimensional wakes are generated for all $R$ in this range.[16~23] In the present experiment, a rectangular plate of 4.6—5.9cm wide and 8.3—8.9cm long was attached at the bottom end of each cylinder to diminish end effects. The plate was inclined to make shedding vortex streets as parallel as possible. This end condition yielded almost two-dimensional flow pattern both in the near and far wakes, as shown in §4.1.

Two series of experiments were carried out using these tanks and cylinders : in series I, the long tank was used, and the side-view flow pattern was visualized using the aluminium dust method with illumination on the vertical plane including the cylinder. We took photographs of this flow pattern every 10 seconds with a 35mm camera fixed at 2.8m ahead of the initial position of the cylinder. The wavelongths and speeds of the primary and secondary vortex streets were measured from these photographs.

In series II experiments, polyethylene particles were mixed with water for flow visualization. The particles had sizes 75—150 $\mu$m in diameter, and were coated with a bond (Alone-alpha) so that their density was almost the same as that of water. They were illuminated horizontally at a height of 25cm above the bottom by sheets of light from two slide projectors. These projectors were placed just outside the side walls of the tank so that they were facing each other. The thickness of the sheet was about 5mm at the position of the model. Movements of the particles in the light sheet were recorded by a video camera. Elapsed time was also recorded on a video image. In experiments using the long tank, the recording and illumination systems mounted on the carriage were

moved at velocioy $U_c \approx 0.2U$, so that the evolution of each vortex region in the primary vortex street could be observed for a long time. Whereas, in experiments using the short tank, the systems were fixed at 1.5m ahead of the initial position of the model. Experiments were repeated over 10 times, and image data having good contrast and adequate particle density were used for the digital image processing described in the next section.

## 3. Digital image processing

In order to see clearly the breakdown and rearrangement of the primary vortex street, we measured velocity and vorticity fields using a particle-tracking technique from the visualized flow field in the series II experiments. This technique is often used for the unsteady wake flow of a bluff body. Its applications to the two-dimensional near wake of a circular cylinder at low Reynolds number were reported by Imaichi : Ohmi[24] and Green & Gerrard.[25] Agüí & Jdménez[26] also used this technique for moderately three-dimensional turbulent flow in the near wake of a cylinder. However, no application to the far wake seems to exist.

In the present work, velocity and vorticity fields were computed from image data by means of the following procedure : when we wanted to obtain the fields at time $T$, two instantaneous images of particles at times $T_1 = T - \Delta T$ and $T_2 = T + \Delta T$ and a track image for the time from $T_1$ to $T_2$ were generated on an image processor (NEXUS 6400) through an 8-bits A/D converter. These three digital images were reduced to binary images with a threshold value. Then original velocity data were computed from the positions of the ends of available pathlines during a small exposure time $2\Delta T$ in the track image. In order to determine the direction of the velocities, we used the two instantaneous images. The value of $\Delta T$ was chosen so that the longest pathline in each track image was composed of a sufficient number of pixels and also was almost straight. The data acquisition with this method was performed automatically by the use of a program on the processor. Here intersecting pathlines and pathlines of particles which appear later than $T_1$ or disappear earlier than $T_2$ were removed automatically, although their ratio was fairly small. We used a few threshold values for each image in order to obtain as many velocity data as possible. We usually obtained 300—600 velocity data for each image. An example of these data is shown by thin lines in Fig. 1.

Here, we define $x$ and $y$ as the coordinates in the longitudinal and transverse directions, respectively, fixed to the cylinder. Their origin is located at the backward edge of the cylinder, and $x$ increases in the downstream direction. Velocities $(u_{i,j}, v_{i,j})$ at a mesh point $(x, y) = (x_i, y_j)$ of a square lattice of spachng $\ell$, which in $0.5d - 0.6d$, were computed from the above volocity data by the interpolation method described below : we first assume that the velocity $(u, v)$ near the mesh point $(x_i, y_j)$ is expressed as

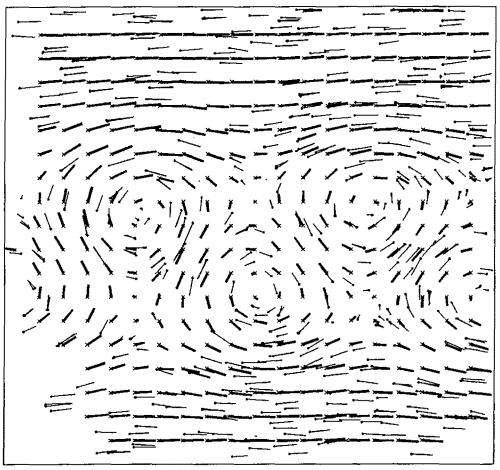

Fig. 1 An example of original velocity data (thin lines) and mesh-point velocities (thick lines) computed from them. $U_c=0.2U$. $R=106$.

$$\begin{cases} u=\alpha_1 x+\beta_1 y+\gamma_1, \\ v=\alpha_2 x+\beta_2 y+\gamma_2, \end{cases} \tag{1}$$

where $\alpha_k$, $\beta_k$, and $\gamma_k$ $(k=1, 2)$ are constants. Then these constants are determined by the least-square approximation from the original velocity data within a circle of radius $D$ around $(x_i, y_j)$. Here $D$ was usually chosen as $1.0d$ or $1.2d$. Therefore, the mesh-point velocity $(u_{i,j}, v_{i,j})$ can be computed from eq.(1). An example of the application of this interpolation method is shown in Fig. 1, where velocities at mesh points are expressed by thick lines. This method works well, as this figure clearly illustrates. Finally, these meshpoint velocities were changed into the values in the reference frame fixed to the cylinder by adding $U-U_c$ to the streamwise component. The vorticity $\omega=\omega_{i,j}$ at a mesh point $(x_i, y_j)$ was computed from the following scheme :

$$\omega_{i,j}=\frac{v_{i+1,j}-v_{i-1,j}}{2\ell}-\frac{u_{i,j+1}-u_{i,j-1}}{2\ell}. \tag{2}$$

From now on, these velocity and vorticity fields and their original velocity data are specified by $L$, the $x$ value of the center of the image taken at the time $T$ in the preceding explanation of data acquisition.

The errors in the above data acquisition and interpolation were estimated by the following two computations : first, the original velocity data modified by adding $U=U_c$ to the streamwise component, say $(u_a, v_a)$ $(a=1, 2, \cdots, N_0)$, were compared with the velocities $(\tilde{u}_a, \tilde{v}_a)$ $(a=1, 2, \cdots, N_0)$ at the same positions obtained by an interpolation of the mesh-point velocities. The variable

$$\sigma=\frac{\sqrt{\frac{1}{N_0}\sum_{\alpha=1}^{N_0}\{(u_\alpha-\tilde{u}_\alpha)^2+(v_\alpha-\tilde{v}_\alpha)^2\}}}{\max_{i,j}\sqrt{(u_{i,j}-U)^2+v_{i,j}^2}}, \tag{3}$$

was computed for each velocity field and original velocity data. Consequently, $\sigma$ was 0.08−0.14 for $L/d\leq 30$, and 0.05−0.10 for $L/d\geq 30$. Another error estimation was made for each velocity field by computing

$$\bar{\sigma}=\frac{\sqrt{\frac{1}{N_m}\sum_{i,j}D_{i,j}^2}}{\max_{i,j}|\omega_{i,j}|}, \tag{4}$$

where summation is over all mesh points of number $N_m$, and

$$D_{i,j}=\frac{u_{i+1,j}-u_{i-1,j}}{2\ell}+\frac{v_{i,j+1}-v_{i,j-1}}{2\ell}, \tag{5}$$

is expected to be close to zero for a two-dimensional flow of an incompressible fluid if $\ell$ is small. We obtained $\bar{\sigma}=0.06-0.08$ for $L/d\leq 30$, and $\bar{\sigma}=0.04-0.08$ for $L/d\geq 30$. These values of $\sigma$ and $\bar{\sigma}$ show moderate accuracy in the near-wake region and higher accuracy in the far-wake region.

## 4. Experimental results

### 4.1. Geometrical configuration of visualized flow field in series I experiments

Figure 2 shows a few typical examples of the side-view flow pattern of the wake field obtained in the series I experiments. We first find that the wake is almost two-dimensional. Moreover, we see a periodic pattern of constant wavelength near the cylinder and one of larger constant wavelength far downstream. It is likely that these two patterns correspond to the primary and

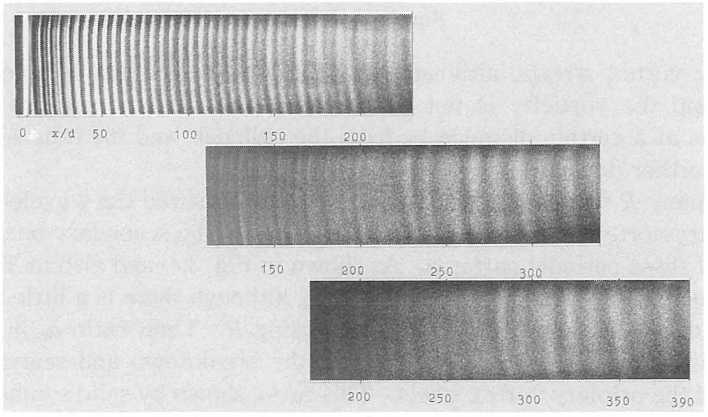


Fig. 2 Side-view flow patterns of the wake visualized by the aluminium dust method.(a)$R=82$

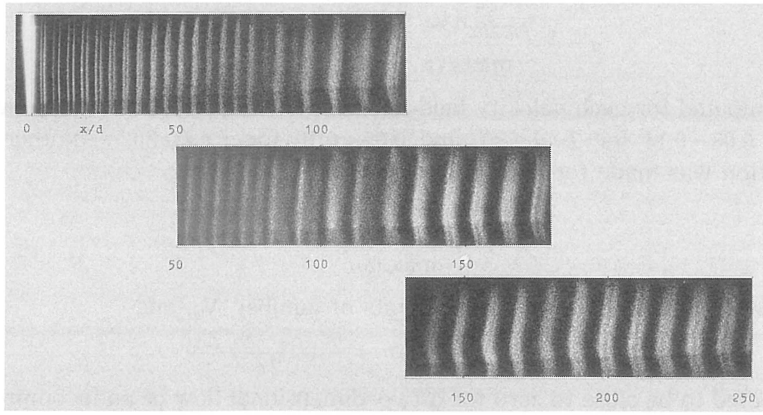


Fig. 2 (b)$R=117$

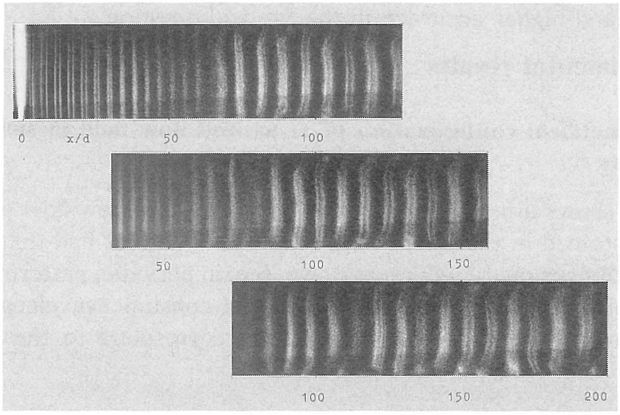


Fig. 2 (c)$R=146$.

secondary vortex streets, although the relation between the lightness in the pattern and the vorticity is not clear. The first periodic pattern becomes ambiguous at a certain distance $x_p$ from the cylinder, and then the second one appears further downstream.

For many $R$ values between 70 and 154, we measured the wavelength $a_1$ of the primary vortex street and the wavelength $a_2$ of the secondary one from the periods of these periodic patterns. As shown in Fig. 3(a) and also in Table 1, $R$ -dependence of $a_1$ is fairly weak, whereas $a_2$, although there is a little scatter in the data, decreases considerably with increasing $R$. Their ratio $a_2/a_1$ is important in discussing the main mechanism in the breakdown and rearrangement process of the primary vortex street. This ratio, shown by solid symbols in Fig. 3(b), decreases with increasing $R$, and ranges from 1.7 to 2.6 for $70<R<154$. There is no indication that this ratio is close to 2 for a wide range of $R$ values.

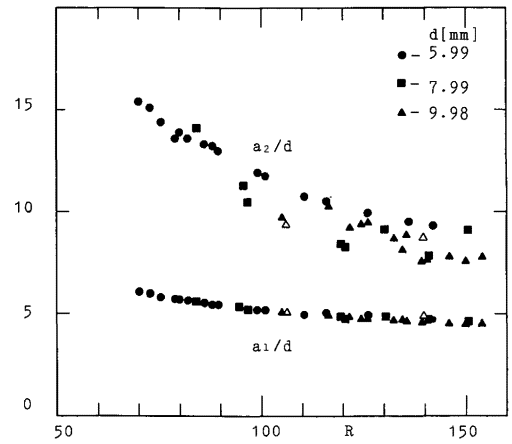


Fig. 3 (a) Wavelength $a_1$ of the primary vortex street, and wavelength $a_2$ of the secondary one.

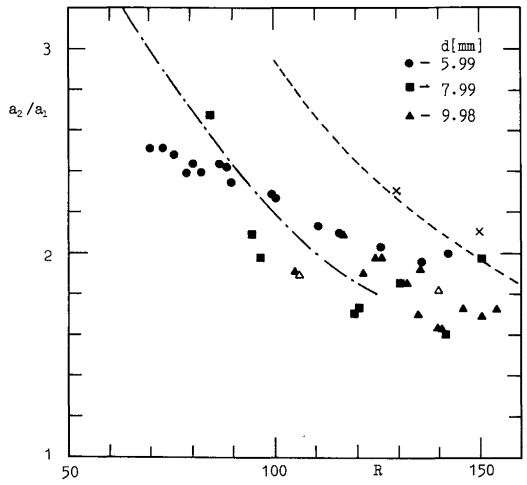


Fig.3 (b) Their ratio $a_2/a_1$. Solid symbols denote the results in series I experiments. △, the result by the digital image processing.
—•—•—, Taneda's result. ———, Matsui & Okude's result. ×, the result by Cimbala et al.

Table 1 Tabulated examples of data for the primary and secondary vortex streets.

| d[mm] | $R$ | $U$[cm/s] | $a_1/d$ | $a_2/d$ | $u_1/U$ | $u_2/U$ | $x_p/10d$ | $F_1$ | $F_2$ |
|---|---|---|---|---|---|---|---|---|---|
| 5.99 | 70 | 1.47 | 6.1 | 15 | 0.13 | 0.035 | 20 | 10 | 4.4 |
| | 73 | 1.54 | 6.0 | 15 | 0.12 | 0.028 | 20 | 11 | 4.7 |
| | 75 | 1.58 | 5.8 | 14 | 0.12 | 0.055 | 20 | 11 | 5.0 |
| | 79 | 1.66 | 5.7 | 14 | 0.13 | 0.041 | 18 | 12 | 5.6 |
| | 80 | 1.64 | 5.7 | 14 | 0.13 | 0.058 | 16 | 12 | 5.4 |
| | 82 | 1.75 | 5.7 | 14 | 0.13 | 0.047 | 17 | 13 | 5.8 |
| | 86 | 1.84 | 5.5 | 13 | 0.15 | 0.047 | 18 | 13 | 6.2 |
| | 88 | 2.08 | 5.5 | 13 | 0.15 | 0.061 | 15 | 14 | 6.2 |
| | 90 | 2.11 | 5.5 | 13 | 0.13 | 0.054 | 16 | 14 | 6.5 |
| | 99 | 2.12 | 5.2 | 12 | 0.15 | 0.062 | 12 | 16 | 7.8 |
| | 101 | 2.17 | 5.2 | 12 | 0.14 | 0.086 | 11 | 17 | 7.8 |
| | 111 | 2.36 | 5.0 | 11 | 0.16 | 0.070 | 10 | 19 | 9.6 |
| | 116 | 1.89 | 5.0 | 11 | 0.17 | 0.069 | 9.6 | 19 | 10 |
| | 126 | 2.07 | 4.9 | 10 | 0.14 | 0.064 | 7.2 | 22 | 12 |
| | 136 | 2.23 | 4.9 | 9.6 | 0.14 | 0.074 | 8.6 | 24 | 13 |
| | 142 | 2.32 | 4.7 | 9.4 | 0.14 | 0.065 | 7.1 | 26 | 14 |
| 7.99 | 84 | 1.02 | 5.6 | 15 | 0.15 | 0.052 | 11 | 13 | 5.3 |
| | 95 | 1.33 | 5.4 | 11 | 0.13 | 0.076 | 14 | 15 | 7.7 |
| | 97 | 1.35 | 5.3 | 11 | 0.15 | 0.081 | 13 | 16 | 8.4 |
| | 119 | 1.44 | 4.9 | 8.4 | 0.14 | 0.087 | 10 | 21 | 13 |
| | 121 | 1.49 | 4.8 | 8.3 | 0.15 | 0.091 | — | 21 | 13 |
| | 131 | 1.61 | 4.9 | 9.1 | 0.12 | 0.095 | 5.2 | 24 | 13 |
| | 141 | 1.70 | 4.8 | 7.7 | 0.13 | 0.077 | 6.8 | 26 | 17 |
| | 150 | 1.82 | 4.6 | 9.1 | 0.16 | 0.080 | 6.9 | 27 | 15 |
| 9.98 | 105 | 1.26 | 5.1 | 9.8 | 0.14 | 0.070 | 12 | 18 | 10 |
| | 117 | 1.41 | 4.9 | 10 | 0.15 | 0.044 | 9.8 | 20 | 11 |
| | 122 | 1.50 | 4.9 | 9.3 | 0.15 | 0.084 | 7.6 | 21 | 12 |
| | 125 | 1.50 | 4.8 | 9.5 | 0.15 | 0.075 | 9.7 | 22 | 11 |
| | 126 | 1.51 | 4.8 | 9.5 | 0.14 | 0.088 | 7.7 | 23 | 12 |
| | 133 | 1.62 | 4.7 | 8.7 | 0.15 | 0.087 | 8.4 | 24 | 14 |
| | 135 | 1.60 | 4.8 | 8.1 | 0.15 | 0.071 | 9.1 | 24 | 15 |
| | 136 | 1.64 | 4.6 | 8.9 | 0.15 | 0.078 | 7.5 | 25 | 14 |
| | 139 | 1.70 | 4.6 | 7.5 | 0.16 | 0.098 | 7.1 | 26 | 17 |
| | 141 | 1.74 | 4.7 | 2.6 | 0.14 | 0.083 | 6.4 | 26 | 17 |
| | 146 | 1.76 | 4.5 | 7.8 | 0.17 | 0.083 | 6.2 | 27 | 17 |
| | 150 | 1.81 | 4.5 | 7.6 | 0.15 | 0.098 | 6.2 | 29 | 18 |
| | 154 | 1.77 | 4.5 | 7.8 | 0.18 | 0.10 | 6.9 | 28 | 18 |

This seems to contradict the scenario of the vortex pairing. The experiments by Taneda[1] yielded the data roughly expressed by a dotted-broken line in Fig. 3(b), whereas Matsui & Okude[27] and Okude[28] obtained the result denoted by a broken line. Both of them show a decrease, similar to ours, in the ratio $a_2/a_1$ with increasing $R$. The ratio measured by Cimbala et al.[4] is also shown by crosses. Taneda's values are similar to ours, whereas the values by Matsui & Okude and by Cimbala et al. are slightly larger.

Next, we measured $u_1$ and $u_2$, the speeds of the first and second periodic patterns relative to the fluid at infinity, from a series of photographs of the flow patterns such as those shown in Fig. 2. As found from Table 1, the speed $u_1$ is $0.12U-0.18U$ for $70<R<154$, and has weak $R$-dependence, whereas $u_2$ roughly increases from $0.03U$ to $0.10U$ with $R$, and is considerably smaller than $u_1$. This result suggests that the primary vortex street moves faster than the secondary vortex treet in the reference frame fixed to the fluid at infinity.

The value of $x_p$, which is expected to be the downstream distance of the position where the primary vortex street breaks down, decreases with increasing $R$, as shown in Fig. 4 (and in Table 1). This tendency is consistent with the results by Taneda[1], by Honji[2], and by Cimbala et al.[4] Honji's result, shown in Fig. 4 by a broken line, gives a little smaller values than ours. This discrepancy may be due to the difference in the flow visualization method (Honji measured $x_p$ on the basis of the streak patterns obtained using the electrolytic precipita-

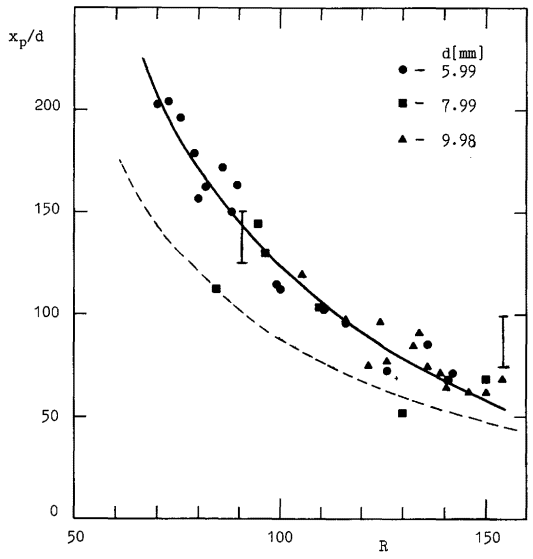


Fig. 4 Dependence of $x_p$ on $R$. Solid symbols denote the results in series I experiments. Solid line shows their rough tendency. ———, Honji's result. I, the result by Cimbala et al.

tion method). The values by Cimbala et al.[4] are also shown in Fig. 4. Although their value for $R=90$ is consistent with ours, that for $R=155$ is a little larger.

Next, we calculated the frequency of the time variation associated with the passage of the vortex streets. That is, the frequencies $f_1$ and $f_2$ within the regions of the primary and secondary vortex streets, corresponding to the variations of signals at a measuring point fixed to the cylinder, were calculated from the formula $f_k=(U-u_k)/a_k (k=1, 2)$. Figure 5 shows that nondimensional frequencies $F_1$ and $F_2$, defined by $F_k=f_k d^2/\nu$ $(k=1, 2)$, increase almost linearly with $R$. The calculation based on the least-square approximation gives the relations

$$F_1=0.22R-5.4,\ F_2=0.16R-7.4, \tag{6}$$

which are expressed by solid lines in Fig. 5. These increases of $F_1$ and $F_2$ are mainly due to the decreases of $a_1$ and $a_2$ with increasing $R$, as found from Table 1. The ratio $F_1/F_2$, shown in Fig. 6, decreases with increasing $R$ and changes over the range between 1.5 and 2.3. This result suggests another problem in the vortex-pairing scenario because the expected ratio is $F_1/F_2=2$.

Matsui & Okude[27] and Okude[28] measured the frequencies of the velocity

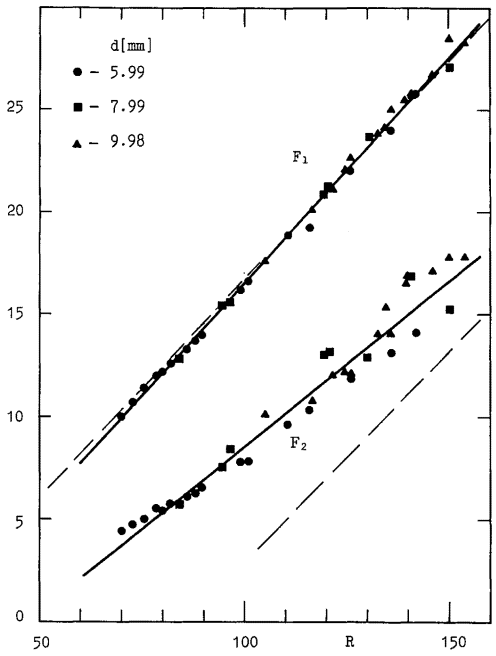


Fig. 5 Nondimensional frequencies $F_1$ and $F_2$ corresponding to the primary and secondary vortex streets. Solid symbols denote the present results. Solid lines show their rough tendency. ———, Matsui & Okude's result.

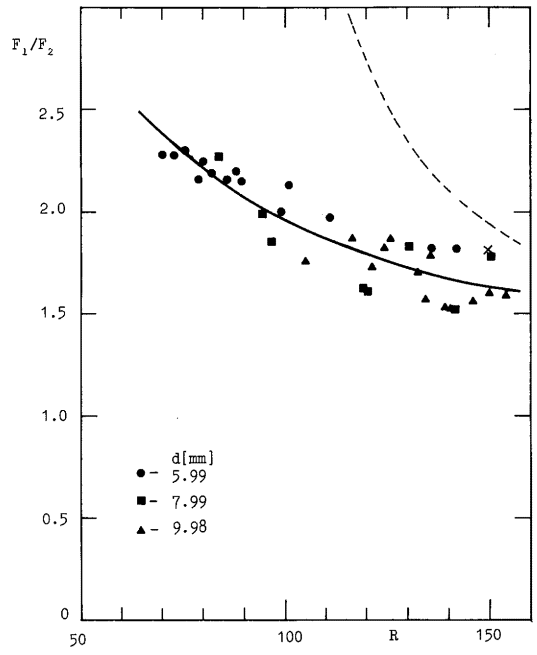


Fig. 6 Dependence of $F_1/F_2$ on $R$. Solid symbols denote the present results. Solid line shows their rough tendency. ———, Matsui & Okude's result. ×, the result by Cimbala et al.

fluctuations in the primary and secondary vortex streets. They also obtained the linear dependences of $F_1$ and $F_2$ on $R$. As found from Fig. 5, their result on $F_1$ agrres well with ours, whereas their $F_2$ value is considerably smaller than ours. Therefore, their ratio $F_1/F_2$, expressed by a broken line in Fig. 6, is appreciably larger than ours, particularly in the low $R$ region. The data by Cimbala et al.[4], expressed by a cross in Fig. 6, lies midway between Matsui & Okude's and our data.

## 4.2. Vorticity fields

Figures 7-10 show the evolution of the vorticity field $\omega(x, y)$ with increasing downstream distance obtained by the digital image processing. In order to specify each vorticity field, we use the distance $L$ in §3. In Figs. 7 and 9, contour lines for positive and negative vorticities are expressed by solid and broken lines, respectively. Here these contour lines are drawn on the basis of the values normalized with the largest absolute value of vorticity of each field, which decreases with increasing $L$. Figures 8 and 10 are perspective views of the vorticity fields shown in Figs. 7 and 9, respectively.

Both Figs. 7 and 8 for $R=106$ and Figs. 9 and 10 for $R=140$ indicate that

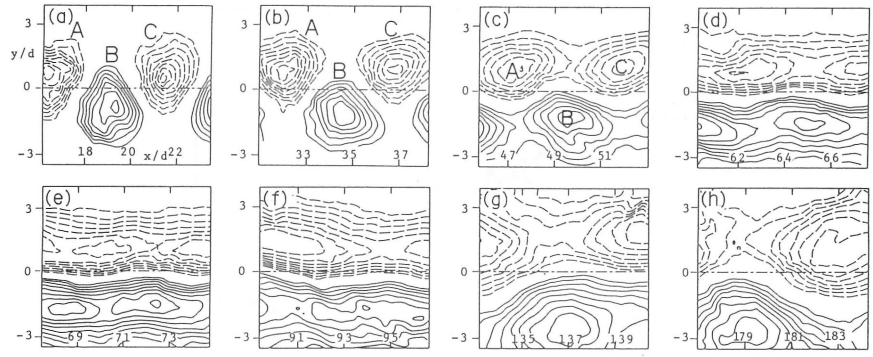


Fig.7 Evoution of vorticity field $\omega(x, y)$ with increasing downstream distance. $R=106$, $U_c=0.2U$. Contour lines for positive vorticity (solid lines) and for negative vorticity (broken lines) are drawn on the basis of the values $\pm 0.2\omega_{max}$, $\pm 0.3\omega_{max}$, $\cdots$, $\pm 0.9\omega_{max}$. Here $\omega_{max}$ is the maximum absolute value of the vorticity for each $L$. (a)$L/d$ $=20.0$, (b) 34.6, (c) 49.2, (d) 63.9, (e) 71.1, (f) 93.0, (g) 136.8, (h) 180.6. A, B, and C are letters assigned to the vortex regions.

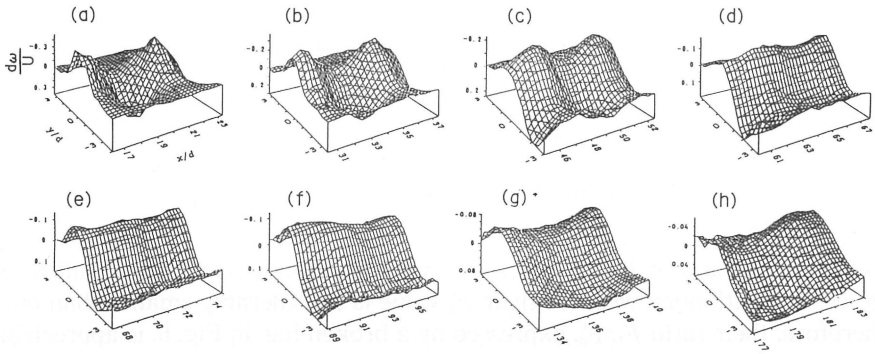


Fig. 8 Perspective view of the vorticity fields shown in Fig. 7.

the primary vortex street evolves into a nearly parallel shear flow, as shown in Figs. 7(e), 8(e), 9(d), and 10(d), before the secondary vortex street of larger scale appears further downstream. This indication agrees with the result by Cimbala et al.[3, 4] In our experiments, even at the downstream distance where the flow field is the closest to a parallel flow, the vorticity field is not completely uniform in the streamwise direction. However, no indication of the vortex pairing is found from this vorticity field.

Matsui & Okude[9] and Okude & Matsui[6] obtained vorticity fields in the far wake using a conditional sampling of the velocities measured by the hot-wire technique. This method, however, is applicable only to regular flow patterns. Therefore, they obtained vorticity fields only until just before the breakdown of the primary vortex street, because its breakdown and rearrangement process

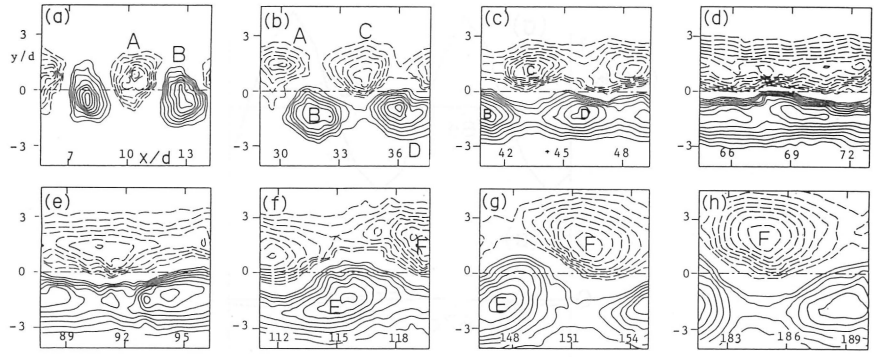


Fig.9 Evoution of vorticity field $\omega(x, y)$ with increasing downstream distance. $R=140$, $U_c=0$. Contour lines are drawn in the similar way as Fig. 7. (a)$L/d=9.9$, (b) 33.3, (c) 45.0, (d) 68.5, (e) 92.0, (f) 115.4, (g) 150. 6, (h) 185.8. A, B, ··· are letters assigned to the vortex regions.

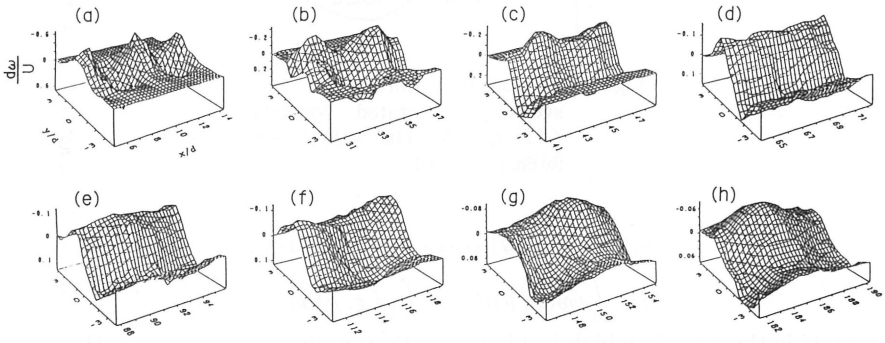


Fig. 10 Perspective view of the vorticity fields shown in Fig. 9.

was a little irregular. The evolution of the primary vortex street shown in Fig. 8 of Okude & Matsui[6] is similar to that shown in Figs. 9(a), (b), and (c).

In order to show the process from the primary to the secondary vortex streets more clearly, we calculated trasversally integrated vorticity $Q(x)$ in each vorticity field. Figure 11 shows the evolution of $Q(x)$ normalized with $Q_N$. Here $Q_N$ is computed by the longitudinal averaging, over all $x's$ in each field, of transversally integrated $|\omega|$. We easily find that in the above process the wake flow goes through a state that is strongly uniform in the $x$ direction.

Next, in order to examine the geometrical configuration of the vortex streets, we calculated the location $(x_0, y_0)$ of the conter of each vortex region from the formula:

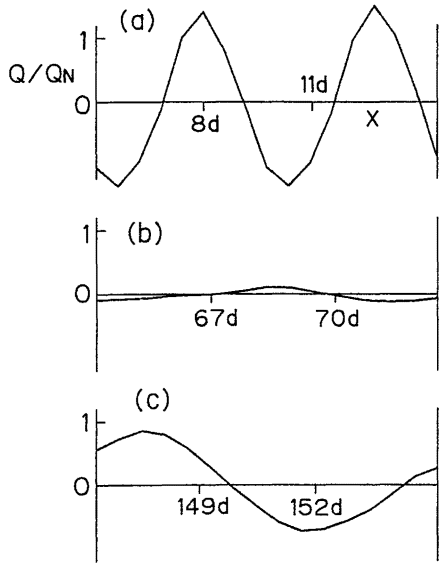


Fig. 11 Evolution of normalized transversally integrated vorticity $Q(x)/Q^N$. $R=140$. (a)$L/d=9.9$, (b) 68.5, (c) 150.6.

$$\begin{cases} x_0=\int_V x\omega(x, y)dxdy/\int_V \omega(x, y)dxdy, \\ y_0=\int_V y\omega(x, y)dxdy/\int_V \omega(x, y)dxdy, \end{cases} \tag{7}$$

where $V$ is the area in which $|\omega|$ is larger than a given value $\gamma\omega_{\max}$. Here $\omega_{\max}$ is the largest $|\omega|$ value in the vortex region, and $\gamma$ is chosen so that $V$ contains only this vortex region. The alteration of $\gamma$ satisfying this condition, between 0.2 and 0.4 for the near wake and between 0.4 and 0.7 for the far wake, gave rise to no significant change in the values of $(x_0, y_0)$. According to these $x_0$ values, we calculated the longitudinal spacings $a_1$ and $a_2$ of vortex regions of the same sign in the primary and secondary vortex streets, respectively. These spacings were also calculated from the $x$ values for which $Q(x)$ takes the extremum. These two methods gave approximately the same spacing values. Consequently, $a_1$ and $a_2$ are almost independent of $x$, and, for $R=140$, $a_1=4.8d$ and $a_2=8.7d$, whereas $a_1=4.9d$ and $a_2=9.3d$ for $R=106$. These values agree well with the results in the series I experiments, as shown in Fig. 3.

Transverse spacings $h_1$ and $h_2$ of neighbouring vortex regions of opposite sign in the primary and secondary vortex streets were also calculated from the $y_0$ values. Figure 12 shows the spacing ratios $h_1/a_1$ in the left side (small $x$) and $h_2/a_2$ in the right side (large $x$). The ratio $h_1/a_1$ at first increases rapidly with

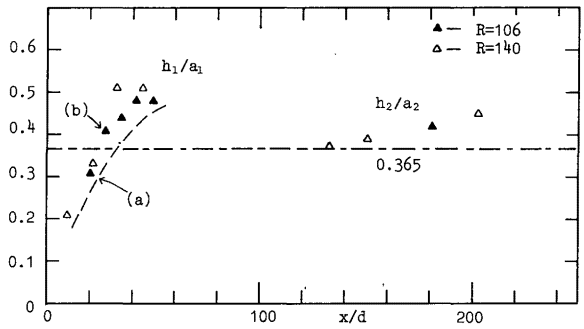


Fig. 12 Change of the spacing ratios $h_1/a_1$ and $h_2/a_2$ with downstream distance. Triangles denote the present results. ———, Okude & Matsui's result.

$x$, and then saturates at a value close to 0.5 before the breakdown of the primary vortex street. Although the ratio $h_2/a_2$ also increases with $x$, its increase rate is fairly small. Okude & Matsui[29] calculated $h_1/a_1$ using three different methods based on the smoke-wire flow visualization or hot-wire anemometry. Their result for $R=80$, 110, and 140, expressed by a broken line in Fig. 12, is similar to ours. Their final value 0.45, however, is a little smaller than our value 0.5. It should be noted that both their results and ours show weak dependence of $h_1/a_1$ on $R$.

Finally, the movements of the vortex regions were examined. In Figs. 7 and 9, their movements are easily noticed since letters (A, B, ···) are assigned to each of them. Their speed in the streamwise direction was calculated according to the $x_0$ values in several vorticity fields. The speed in the primary vortex street relative to the fluid at infinity is almost independent of $x$, and, for $R=140$, is $0.18U-0.19U$, and $0.15U-0.18U$ for $R=106$. These values are a little larger than $u_1$ introduced in §4.1, which is $0.13U-0.16U$ for $R\approx140$ and $0.14U-0.16U$ for $R\approx106$. On the other hand, the vortex regions in the secondary vortex street move at the lower speed of $0.05U-0.10U$ for these $R$ values. This speed is consistent with the $u_2$ value shown in Table 1. Okude & Matsui[30] obtained the speed $0.14U$ for the primary vortex street with $R=140$ from visualized flow patterns and the data of velocity fluctuation. This value is consistent with our $u_1$ value.

## 5. Breakdown of primary vortex streets

In this section, we will discuss in detail the process from the primary vortex street to the nearly parallel shear flow, described in §4. In this process, the effect of viscous diffusion does not seem dominant. This suggestion is based on the following rough estimations : the time required for the diffusion of vorticity over the representative longitudinal length $a_1$ is estimated to be $a_1^2/\nu$, whereas the

estimated time spent for the evolution of the vortex street to the parallel flow in the experiments is $x_p/U$. The ratio between these time scales is expressed as $(a_1^2/\nu)/(x_p/U)=(a_1/d)^2R/(x_p/d)$, which is 10−50 according to the data in Table 1. Therefore, the viscous diffusion seems unimportant in this process.

Durgin & Karlsson[7] in the discussion of their experimental results on the decelerated wake, proposed the following explanation, based on the inviscid theory, of the process from the primary vortex street to the stationary wake flow. If we assume the Kármán type staggered arrangement of two rows of point vortices of strengths $\pm\Gamma$, shown in Fig. 13(a), then the velocity $(u, v)$ at a point $(x, y)$ near a point vortex in the lower row located at $(x_0, y_0)$, induced by all other vortices, is expressed by

$$\begin{cases} u=-\dfrac{\Gamma}{2a_1}T-\dfrac{\pi\Gamma}{6a_1^2}(3T^2-2)\tilde{y}+O(|\tilde{\boldsymbol{r}}|^2), \\ v=-\dfrac{\pi\Gamma}{6a_1^2}(3T^2-2)\tilde{x}+O(|\tilde{\boldsymbol{r}}|^2), \end{cases} \tag{8}$$

where $\tilde{x}=x-x_0$, $\tilde{y}=y-y_0$, $\tilde{\boldsymbol{r}}=(\tilde{x}, \tilde{y})$, $T=\tanh(\pi h_1/a_1)$, $h_1$ is the distance between the two rows, and $a_1$ is the spacing of the vortices of the same sign. Therefore, for $T>\sqrt{2/3}$, that is for $h_1/a_1>0.365$, we have the induced velocity

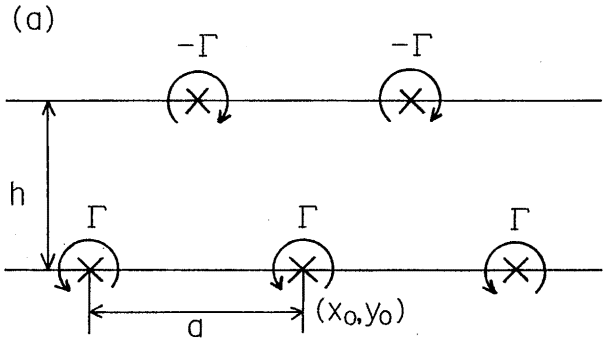


Fig. 13 (a) Kármán type vortex street.

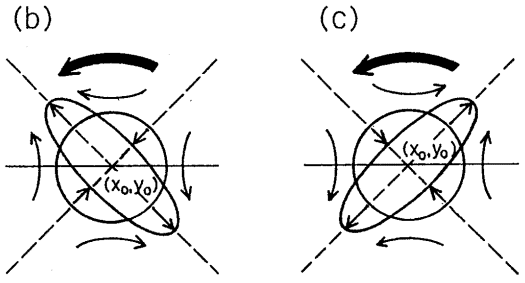


Fig. 13 (b), (c) Distortion of a vortex region for (b) $h_1/a_1>0.365$, (c) for $h_1/a_1<0.365$.

field expressed by thin arrows in Fig. 13(b) near $(x_0, y_0)$. Here the effect of the collective motion at the velocity $(-\Gamma T/2a_1, 0)$ is removed, and $\Gamma$ is assumed to be positive. Therefore, if, instead of the point vortex, we consider a circular vortex region of small area with center at $(x_0, y_0)$, the latter will be distorted into an ellipse in the way shown in Fig. 13(b). In contrast, if $T<\sqrt{2/3}$, that is if $h_1/a_1<0.365$, a mirror-image distortion will occur, as found from Fig. 13(c). Next, this distorted vortex region will rotate in the direction expressed by thick arrows in Figs. 13(b) and (c), owing to the effect of the velocity induced by the vorticity within the region. Thus, the major axis of the region will tend to turn counterclockwise toward the longitudinal direction if $h_1/a_1>0.365$. Therefore, if we consider a vortex street composed of finite-area vortexregions whose centers satisfy the relation $h_1/a_1>0.365$, we obtain the following suggestion : this vortex street will evolve to an approximately parallel shear flow if each region becomes sufficiently slender so that it overlaps with neighbouring regions of the same sign. On the other hand, for $h_1/a_1<0.365$, similar discussion suggests the preservation of the initial localized vortex structure. Therefore, if we consider a situation in which the ratio $h_1/a_1$ increases with time (or with downstream distance) from a value smaller than 0.365, the vortex street can evolve into a nearly parallel shear flow after the ratio increases beyond 0.365. This is the scenario by Durgin & Karlsson[7], and was used to explain the result of their experiments in which $h_1/a_1$ seems to increase with downstream distance because $a_1$ decreases owing to the deceleration of the flow.

Of course, this scenario is not perfect, as they themselves admitted. For example, the above two kinds of induced velocities must be taken into account simultaneously, and also expression (8) is not a good approximation when each vortex region has a fairly large area and is distorted to a considerable extent. However, Tsuboi & Oshima[13] obtained a numerical result which is consistent with this scenario. That is, using the discrete vortex method, they investigated the evolution of a Kármán vortex street composed of circular vortex regions of uniform vorticity. They then found the transition to a nearly parallel flow (called merging in their paper) when both $h_1/a_1$ is larger than a value roughly estimated as 0.4—0.5, and the area of the vortex region is not so small compared with $a_1^2$. This result suggests that Durgin & Karlsson's scenario is valid even for the evolution of a vortex street composed of vortex regions of fairly large area, although the threshold value of $h_1/a_1$ may be a little larger than 0.365.

In the primary vortex street of the present work, each vorticity region has neither circular shape nor uniform vorticity at any time, as found from Figs. 7 -10. However, since this vortex street also is such that $h_1/a_1$ increases with the downstream distance as shown in Fig. 12, Durgin & Karlsson's scenario may be applicable to it. Figures 7 and 9 give some indication of the distortion and turning of vortex regions which is consistent with the scenario. Definite conclusion is, however, not obtained from these figures.

In order to examine this problem in more detail, we carried out a numerical calculation using the inviscid discrete vortex method. In the calculation, the initial configuration of point vortices was determined in the following way : we first chose a part of the vorticity field containing a pair of vortex regions of opposite sign. In approximating the nonuniform vorticity field within each vortex region by the aggregation of many point vortices, we used this criterion : "the point vortices have the same strength, and their number density is proportional to the vorticity." In the results shown below, each vortex region was approximated by the aggregation of about 200 point vortices. As a typical initial vorticity field representing the case with small $h_1/a_1$, we chose the field containing the vortex regions B and C in Fig. 7(a). Another field containing two vortex regions of opposite signs obtained for $L/d=27.3$ (not shown in Fig. 7) was also used for the case with large $h_1/a_1$. These two fields correspond to (a) and (b) in Fig. 12. We then assumed for these vortex regions a periodic configuration in the $x$ direction with a period $a_v=2\,|x_{01}-x_{02}\,|$, where $x_{01}$ and $x_{02}$ are the $x_0$ values of the original two vortex regions calculated from (7). In the

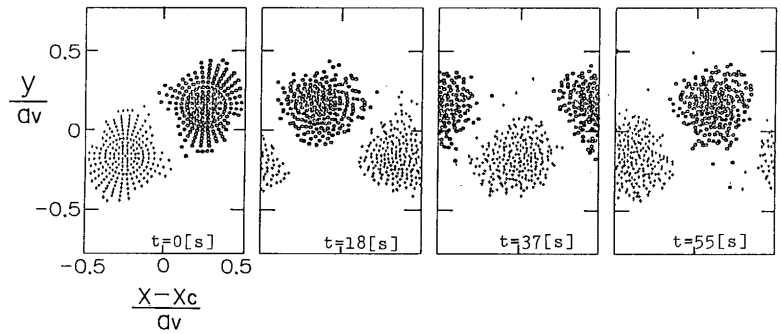


Fig. 14 Evolution of vortex street composed of vortex regions each approximated by $N$ point vortices. $x_c=(x_{01}+x_{02})/2$. (a)$h_1/a_1=0.31$, $N=214$.

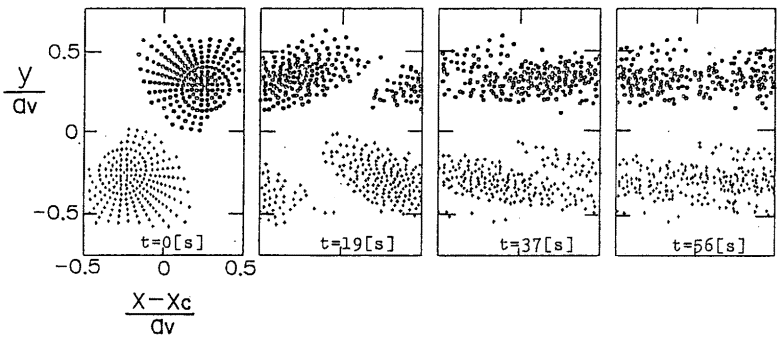


Fig 14 (b) $h_1/a_1=0.41$, $N=202$.

numerical integration of the equation governing the motion of the point vortices, we employed the Euler's scheme of the second order accuracy with a time step corresponding to 0.09 sec.

Figure 14 shows the evolution of the vortex street composed of the above vortex regions with the time $t$. Here only the range of one period in the $x$ direction is shown. As found from Fig. 14(a), when $h_1/a_1$ is small (0.31), the initial vortex regions remain isolated from each other. In contrast to this, when $h_1/a_1$ is large (0.41), the vortex regions amalgamate to form a nearly parallel shear flow, as shown in Fig. 14(b). This latter behaviour is similar to the experimental results shown in Fig. 7. Moreover, the time required for the evolution from the vortex-street state to the nearly parallel flow in the inviscid calculation of Fig. 14(b) is similar to that in the experiment shown in Fig. 7. That is, in the experiment the vortex regions used as the initial condition in Fig. 14(b) evolve into the nearly parallel flow shown in Fig.7(e) after about 60 sec., and the corresponding calculation of Fig. 14(b) gives a similar evolution time to this kind of flow. Incidentally, although the evolution time from the first figure to the last one in Fig. 14(a) is close to the time from Fig. 7(a) to Fig. 7(d), we see noticeable difference between the vorticity field in Fig. 7(d) and that in the last figure of Fig. 14(a).

It is suggested from the results in this section that the breakdown process from the primary vortex street to the nearly parallel flow is basically explained by Durgin & Karlsson's scenario, which is based on the inviscid theory. The viscous effect seems unimportant in the breakdown process, although it probably contributes to the increase in $h_1/a_1$. Furthermore, the results shown in Fig. 14 suggest that the threshold value of $h_1/a_1$ for the occurrence of the breakdown is less than 0.41 in the present case of the large-area nonuniform vortex regions. However, in the experiment, the $h_1/a_1$ value reaches about 0.5 just before the breakdown, as shown in Fig. 12. This large final value may be due to the continuous increase in $h_1/a_1$ during the time spent for the distortion and the turning of the vortex regions.

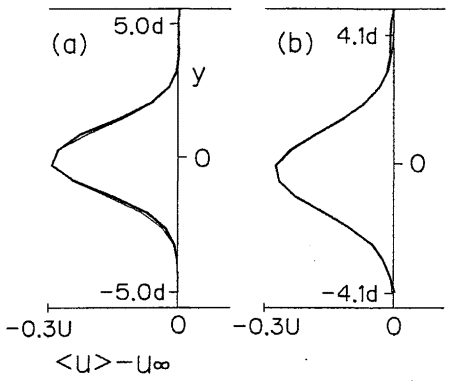


Fig. 15 Averaged longitudinal velocity profiles (thick lines) when the flow field is closest to a parallel flow, and best-fitted Gaussian profiles (thin lines). (a)$R=140$, $L/d=68.5$, (b) $R=106$, $L/d=71.1$.

## 6. Formation of secondary vortex streets

As shown in §4, a nearly parallel flow is observed before

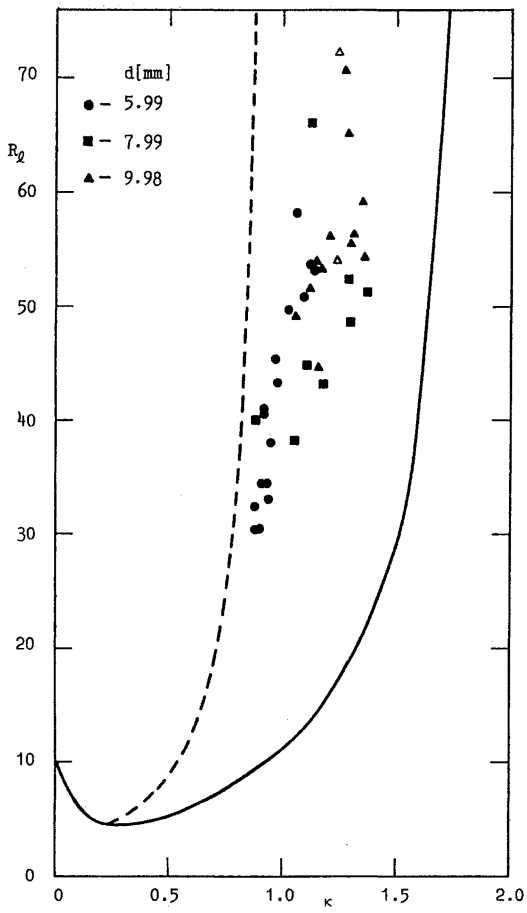


Fig. 16 Comparison of the nondimensional wavenumber of the secondary vortex street with the result in the linear stability theory by Fujimura et al. Open symbols denote the results from the digital image processing, and solid symbols from the data in series I experiments. ———, neutral stability curve. ——, the most unstable mode.

the secondary vortex street appears far downstream. Therefore, it seems reasonable to predict that the formation of this vortex street is due to the instability of the parallel flow, as suggested by Taneda[1] and by Cimbala et al.[3, 4] In order to examine this prediction, we calculated the linear stability of the parallel flow.

Figure 15 shows the $y$-dependence of the longitudinal velocities $<u>$ averaged over all $x$'s in the velocity fields closest to a parallel flow. These velocity profiles are well approximated by the Gaussian profile :

$$u(y)=u_\infty-u_0\exp(-q^2y^2), \tag{9}$$

where $u_\infty$ is the value of $<u>$ for sufficiently large $|y|$, and is close to $U$. Also, for $R=140$, $u_0=0.30U$ and $q=0.58/d$ (Fig. 15(a)), and $u_0=0.18U$ and $q=0.55/d$ for $R=106$ (Fig. 15(b)). Therefore, the local Reynolds number $R_\ell$ based on $u_0$ and $q^{-1}$ is 72 for $R=140$ and 54 for $R=106$.

The linear stability of the wake profile (9) was computed by Fujimura et al.[31] using the expansion of dependent variables by the Chebyshev polynomials. Their results are shown in Fig. 16, where a solid line expresses neutral stability, and a broken line denotes the nondimensional wavenumber $\varkappa=2\pi/q\lambda$ of the most unstable mode for each $R_\ell$. Here $\lambda$ is the wavelength of each mode.

The values of $\varkappa$ corresponding to the wavelength of the secondary vortex street and $R_\ell$ of the nearly parallel flow in the experiments are also shown in Fig. 16. Here open symbols denote the result from the digital image processing. That is, $R_\ell$ was calculated from the velocity profiles shown in Fig. 15, and also the values of $a_2$ shown in §4.2 were used as $\lambda$ in the calculation of $\varkappa$. The data expressed by solid symbols were estimated from the results in the series I experiments in the following way : first, the $y$ coordinate giving the largest vorticity in the Gaussian profile (9), $y=y_v\equiv-1\sqrt{2}q$, is assumed to be the same as the $y$ coordinate of the center of the positive vortex region in the primary vortex street just before its breakdown. Next, if we use the result in §4 that $h_1/a_1\approx0.5$ just before the breakdown, we can estimate $q$ from the formula $0.5a_1/2=-y_v$ using the $a_1$ value at that time. Furthermore, the velocity defect $u_0$ in (9) is estimated from the assumption that the velocity at $y=y_v$ in (9) is equal to the velocity of the primary vortex street just before its breakdown. Using these values of $q$ and $u_0$, and the values of $a_2$ shown in Table 1 as $\lambda$, we can estimate $(\varkappa, R_\ell)$. As shown in Fig. 16, these estimated values are consistent with the data from the digital image processing, in spite of the several assumptions made.

The $R_\ell$ values in the experiments are always much larger than the critical $R_\ell$ value 4.512 in the theory. Furthermore, although the wavelength of the secondary vortex street is always within the unstable region in the theory, it is considerably smaller than that of the most unstable mode. One possible explanation of this discrepancy is that the actual flow field is not exactly parallel and changes slowly in the downstream direction in contrast to the theoretical assumption.

## 7. Discussion and conclusions

We carried out two series of experiments on the breakdown and the rearrangement of the primary vortex street using the aluminium dust method and the digital image processing of the visualized flow fields. Consequently, we

obtained the following results : for $70<R<154$, by appropriately controlling end conditions, two-dimensional vortex streets are observed both in the near and far wakes. Furthermore, the primary vortex street breaks down into a nearly parallel shear flow of Gaussian profile at a certain downstream distance, before a secondary vortex street of larger scale appears further downstream. This breakdown process can be explanined as the evolution of vortex regions of an inviscid fluid if we invoke the observation that the distance between the two rows in the primary vortex street increases with the downstream distance (the Durgin & Karlsson's scenario). That is, the viscous effect is not dominant in this process. Numerical computations with the discrete vortex method also support this explanation. The wavelength of the secondary vortex street is a little smaller than that of the most unstable mode in the linear stability theory applied to the above nearly parallel flow. The ratio of the wavelength of the secondary vortex street to that of the primary vortex street decreases with increasing $R$, and ranges from 1.7 to 2.6. Moreover, the speeds of the vortex streets relative to the fluid at infinity are about $0.12U-0.19U$ and $0.03U-0.10U$ for the primary and secondary vortx streets, respectively.

In contrast to the present work, a few experimets on the evolution of the primary vortex street in the far wake were carried out under controlled forcings. In the experiments by Matsui & Okude[9] and Okude & Matsui[6], a disturbance was introduced into the wake by a loudspeaker driven with half the frequency of the velocity fluctuation in the primary vortex street. They found that the flow pattern and velocity fluctuation in the secondary vortex street are made more regular by the disturbance. Using a conditional sampling of the velocities, they also obtained the evolution of the vorticity field suggesting the vortex pairing (merging). Nakano & Rockwell[10] examined the behaviour of the wake of a transvernally oscillated cylinder for $R=136$. When the oscillation is purely sinusoidal with a frequency close to the inherent frequency of vortex formation, they observed a regular vortex pattern (locked-in response) in the near wake and obtained a result indicating the decay of the vortical structure at least until downstream distance $40d$. In contrast, when the oscillation amplitude is modulated so that it includes subharmonic frequency, they observed a substantial distortion of the vortex pattern leading to an increase in wavelength between the principal vortical structures in the region of downstream distance $20d-35d$. These results imply a significant effect of the subharmonic perturbation on the evolution of the primary vortex street in the far wake. Therefore, since there is no particular reason for the selective generation of subharmonic disturbance in the presnt experiments, there is no contradiction in the fact that our results, which do not suggest vortex pairing, differ from those of Matsui & Okude.

There are also a few theoretical investigations related to the evolution of the vorticity field in the far wake. Aref & Siggia[11] numerically examined the evolution of two parallel vortex sheets of opposite sign with sinusoidal perturba-

tion of wavelength $\lambda_p$. Here a discrete vortex method was used under the assumption of nearly inviscid dynamics. They found that a vortex street of longitudinal spacing $\lambda_p$ emerges for $h/\lambda_p \geq 0.3$, where $h$ is the sheet separation. They also observed for $h/\lambda_p > 0.6$ the transition of this vortex street to a new metastable vortex street of longitudinal spacing $2\lambda_p$ through the pairing of vortex regions of the same sign. Although this first vortex street has a ratio of the transverse spacing to the longitudinal spacing larger than 0.365, its evolution into a nearly parallel flow is not reported, as it is in the Durgin & Karlsson's secenario. One possible explanation of this difference is that each vortex region in the first vortex street is too localized to obey this scenario. This explanation is based on the observation by Tsuboi & Oshima[13] that sufficient extents of the vortex regions are necessary for the evolution into a nearly parallel flow. Meiburg[12] also numerically examined the evolution of the two parallel vortex sheets. In his simulations with an initial perturbation composed of a basic mode of wavelength $\lambda_p = h/0.48$ and its subharmonic of wavelength $2\lambda_p$, only the vortex pairing process was reported during the transition from the vortex street of wavelength $2\lambda_p$. This result also may be due to the insufficient extent of the vortex regions in the first vortex street.

Another related theoretical investigation was carried out by Maekawa et al.[14] They studied the transition mechanism in a spatially developing wake by means of direct numerical simulations of a viscous flow. In their simulations, the inlet flow was forced with a fundamental mode alone in their Case 1, and forced with a fundamental mode and its first and second subharmonics in their Case 3. In Case 3 with $R=200$, they found that a vortex street first appears at a certain downstream distance and is then significantly distorted by the presence of the subharmonics, suggesting an early stage of the vortex pairing. However, apart from the subharmonic aspect of the distortion, the spatial development of the vorticity field shown in their Fig. 6 seems consistent with the Durgin & Karlsson's scenario, That is, the distortion and turning of each vortex region are similar to those in this scenario. Also an increase in the spacing ratio with downstream distance is expected, because a gradual increase in the half-value width of the mean velocity profile is reported. Their other simulation for Case 1, with $R=600$, showed that a regular vortex street formed at a certain downstream distance stays isolated and does not experience further distortion. The spacing ratio of the vortex street, measured from their Fig. 3, takes a constant value of 0.37 for a sufficiently large downstream distance. The results of these two simulations suggest that if a simulation for Case 1 with $R=200$ were carried out, a spatial development to a nearly parallel flow would be observed, owing to the downstream increase in the spacing ratio, as in our experimental result. Unfortunately, however, no result for the above case is shown in their paper.

Finally, aside from the comparison with the experiments, the dependence of the time development of the vortex street composed of finite-area vortex regions of nonuniform vorticity on their shape and on their vorticity distribution

is an interesting theoretical subject. Some results on this subject will be shown in the near future.

**Acknowledgement**

We would like to thank Miss S. Hoshino and Mr. K. Ishii for their technical assistance.

**References**

1) Taneda, S.: *Downstream development of wakes behind cylinders*, J. Phys. Soc. Japan **14** (1959) 843.
2) Honji, H.: *Downstream Persistence of Regular Vortex Streets*, J. Phys. Soc. Japan **55** (1986) 2897.
3) Cimbala, J. M., Nagib, H. M. and Roshko, A.: *Wake instability leading to new large scale structures downstream of bluff bodies*, Bull. Am. Phys. Soc. **26** (1981) 1256.
4) Cimbala, J. M., Naggd, H. M. and Roshko, A.: *Large structure in the far wakes of two-dimensional bluff bodies*, J. Fluid Mech. **190** (1988) 265.
5) Matsui, T. and Okude, M.: *Vortex pairing in a Kârmân vortex street*, In *Proc. Seventh Binennial Symposium on Turbulence, Rolla, Missouri,* (1981).
6) Okude, M. and Matsui, T.: *Vorticity distribution of vortex street in the wake of a circular cylinder*, Trans. Japan Soc. Aero. Space Sci. **33** (1990) 1.
7) Durgin, W. W. and Karlsson, S. K. F.: *On the phenomenon of vortex street breakdown* , J. Fluid Mech. **48** (1971) 507.
8) Gursul, I., Lusseyran, D. and Rockwell, D.: *On interpretation of flow visualization of unsteady shear flows* ,Exp. Fluids **9** (1990) 257.
9) Matsui, T. and Okude, M.: *Formation of the secondary vortex street in the wake of a circular cylinder*, In *Structure of Complex Turbulent Shear Flov, IUTAM Symposium, Marseille, 1982,* (eds. R. Dumas and L. Fulachier, Springer, 1983) p. 156.
10) Nakano, M. and Rockwell, D.: *The wake from a cylinder subjected to* amplitude-modulated excitation, J. Fluid Mech. **247** (1933) 79.
11) Aref, H. and Siggia, E. D.: *Evolution and breakdown of a vortex street in two dimensions*, J. Fluid Mech. **109** (1981) 435.
12) Meiburg, E.: *On the role of subharmonic perturbations in the far wake*, J. Fluid Mech. **177** (1987) 83.
13) Tsuboi, K. and Oshima, Y.: *Numerical study of two-dimensional vortex street*, In *Proc. Computational Fluid Dynamics, Tokyo, 1935,* (ed. K. Oshima, 1985) p. 230.
14) Maekawa, H., Mansour, N. N. and Buell, J. C.: *Instability mode interactions in a statially developing plane wake*, J. Fluid Mech. **235** (1992) 223.
15) Karasudani, T., Funakoshi, M. and Oikawa, M.: *Breakdown and rearrangement of vortex streets in a far wake*, J. Phys. Soc. Japan **58** (1989) 1497.
16) Slaouti, A. and Gerrard, J. H.: *An experimental investigation of the end effects on the wake of a circular cylinder towed through water an low Reynolds numbers*, J. Fluid Mech. **112** (1981) 297.
17) Williamson, C. H. K.: *Defining a universal and continuous Strouhal-Reyonolds number relationship for the laminar vortex shedding of a circular cylinder*, Phys. Fluids **31** (1988) 2742.

18) Williamson, C. H. K.: *Oblique and parallel modes of vortex shedding in the wake of a circular cylinder at low Reynolds numbers*, J. Fluid Mech. **206** (1989) 579.
19) Hammache, M. and Gharib, M.: *A novel method to promote parallel vortex shedding in the wake of a circular cylinder*, Phys. Fluids A **1** (1989) 1611.
20) Hammache, M. and Gharib, M.: *An experimental study of the parallel and oblique vortex shedding from circular cylinders*, J. Fluid Mech. **232** (1991) 567.
21) Eisenlohr, H. and Eckelmann, H.: *Vortex splitting and its consequences in the vortex street wake of cylinders at low Reynolds number*, Phys. Fluids A **1** (1989) 189.
22) Konig, M., Eisenlohr, H. and Eckelmann, H.: *The fine structure in the Strouhal -Reynolds number relationship of the laminar wake of a circular cylinder*, Phys. Fluids A **2** (1990) 1607.
23) Lee, T. and Budwig, R.: *A study of the effect of aspect ratio on vortex shedding behind circular cylinders*, Phys. Fluids A **3** (1991) 309.
24) Imaichi, K. and Ohmi, K.: *Numerical processing of flow-visualization pictures—measurement of two-dimensional vortex flow*, J. Fluid Mech. **129** (1983) 283.
25) Green, R. B. and Gerrard, J. H.: *Vorticity measurements in the near wake of a circular cylinder at low Reynolds numbers*, J. Fluid Mech. **246** (1993) 675.
26) Agui, J. H. and Jimenez, J.: *On the performance of particle tracking*, J. Fluid Mech. **185** (1987) 447.
27) Matsui, T. and Okude, M.: *Rearrangement of Kármân vortex street at low Renolds numbers, XVth International Congress of Theoretical and Applied Mechanics, University of Toronte, August, (1980) p. 1.*
28) Okude, M.: *Rearrangement of Kármân vortex street*, Trans. Japan Soc. Aero. Space Sci. **24** (1981) 95.
29) Okude, M. and Matsui, T.: *Correspodence of velocity fluctuations to flow patterns in a Kármân vortex street at low Reynolds numbers*, Trans. Japan Soc. Aero. Space Sci. **30** (1987) 80.
30) Okude, M. and Matsui, T.: *Vorticity distribution of vortex street in the wake of a circular cylinder*, Japan Soc. Aero. Space Sci. **37** (1989) 582.
31) Fujimura, K., Yanase, S. and Mizushima, J.: *Modulational instablity of plane waves in a two-dimensional jet and wake*, Fluid Dyn. Res. **4** (1988) 15.

(Received October 12,1993)